Influence of misorientation on graphene Moiré patterns

Marie Smirman,[1] Doaa Taha,[2] Arunima K. Singh,[3] Zhi-Feng Huang,[2] and K. R. Elder[1]

[1]*Department of Physics, Oakland University, Rochester, Michigan 48309, USA*

[2]*Department of Physics and Astronomy, Wayne State University, Detroit, Michigan 48201, USA*

[3]*Materials Science and Engineering Division, National Institute of Standards and Technology, Gaithersburg, Maryland 20899, USA*

In this work the influence of film-substrate misorientation on the strain-induced ordering of graphene films on various metallic surfaces is examined using a mesoscopic continuum model and first-principles atomistic calculations. The periodicity and free energy of the Moiré patterns that emerge are studied as a function of film-substrate adhesion strength for misfit strains far from and close to an incommensurate-commensurate phase transition. Interestingly the lowest energy states are found to be at small but finite misorientation even though these states have a higher domain wall density than the zero-misorientation states. First-principles density functional theory calculations are used to connect the results with experimental findings in graphene epitaxy. This combination of mesoscopic and atomistic approaches can be applied to the study of a wide range of strained 2D material systems including the III-nitride monolayer systems.

I. INTRODUCTION

The ordering of two-dimensional (2D) thin films on compact crystalline surfaces has been a topic of great interest for decades. From a fundamental point of view the coupling between the film and substrate often leads to strain induced instabilities that give rise to interesting self-organized spatial patterns that are delineated by regions of commensurability between the adatoms and substrate separated by incommensurate domain walls. Many studies have been conducted to understand the emergence of such patterns and the nature of incommensurate-commensurate (IC) phase transitions. Examples include studies of IC transitions in Kr on graphite [1], the ordering of reactants on patterned surfaces [2], the organization of 2D vacancy islands on heterogeneous metal interfaces [3,4], and surface patterning in heteroepitaxial systems [5–12]. These phenomena are driven by the subtle interplay of adhesion and strain energy contributions. From a technological point of view the resulting film patterns often alter magnetic, electronic, catalytic, and transport properties of the system. Most recently a great deal of research has been driven by the finding that 2D graphene sheets can be obtained from monolayer carbon films grown epitaxially on metallic surfaces [13–23].

Interest in graphene-type 2D materials arises from their extraordinary electronic and mechanical properties and the potential for a myriad of electronic device applications such as field effect transistors, microwave and terahertz photonics, sensors, and supercapacitors [24–26]. However the development of such devices has been hindered by the difficulty in producing large scale defect-free samples in a low-cost and reliable fashion [14,26]. Perhaps the most reliable growth method for large scale sheets is chemical vapor deposition which typically leads to polycrystalline films that contain many defects and grain boundaries [27]. It is thus apparent that predicting and controlling the growth of such films is of both technological and fundamental importance.

Two of the crucial factors controlling the 2D material heteroepitaxy are the effects of the film-substrate adhesion strength and mismatch strain which greatly influence the growth and the resulting properties of the system. A variety of substrates have been adopted in experiments, but a systematic understanding of the corresponding effects is still lacking. In this work different film-substrate systems are characterized via their distance from the IC phase transition of film patterns, such that system structural properties can be efficiently identified and predicted.

A specific property examined here is the role that film-substrate misorientation plays in the ordering of a 2D honeycomb film on compact fcc (111) surfaces of triangular symmetry, as would be relevant for graphene on many metallic substrates. The role of misorientation is particularly important for controlling the growth of graphene films as the film-substrate coupling is often quite weak (on the order of meV/Å^2) and thus it is possible for graphene to nucleate and grow in various lateral orientations with respect to the substrate. However, the corresponding mechanisms of film misalignment are still poorly understood, given large length scales of the resulting ordering patterns that are far beyond the accessible range of atomistic modeling methods [e.g., molecular dynamics and density functional theory (DFT)]. In addition, these atomistic methods usually require *a priori* knowledge of film orientation, which impedes the study of misaligned, noncommensurate structures and patterns.

Here a complex amplitude version of the phase field crystal (APFC) model is used to examine and predict the properties of Moiré patterns in 2D films of various misorientations. This APFC approach solves the critical issue of large length scales by allowing the examination of systems up to 19.6 μm × 33.9 μm size. Two specific film-substrate misfit strains that are representative of graphene epitaxy are studied in detail. They correspond to two of the most commonly used substrates in experiments, Cu(111) and Pt(111), and importantly, represent two distinct limits, one (Cu) close to the IC phase transition and the other (Pt) far from it. To place this work in context, first-principles DFT calculations are also conducted to parametrize and compare the results with experimental work, leading to a combination of APFC and DFT studies across atomistic to micron scales.

II. AMPLITUDE PHASE FIELD CRYSTAL MODEL

The starting point of the PFC model is a free energy functional of the dimensionless atomic number density n, written as $F = F_{PFC} + F_{surf}$, where F_{PFC} is the traditional PFC free energy as described in many prior publications [28–30], and F_{surf} represents the coupling of the density field to a rigid substrate potential V, which for simplicity is given by $F_{surf} = \int d\vec{r} V n$. In the corresponding complex amplitude formulation, $n = \sum_{kl} \eta_{kl} \exp(i\vec{G}_{kl}^s \cdot \vec{r}) + $ c.c., where $G_{kl}^s = \alpha G_{kl}^f$ given a misfit strain $\varepsilon = 1 - \alpha$, $\vec{G}_{kl}^f = k\vec{q}_1 + l\vec{q}_2$ with $(\vec{q}_1, \vec{q}_2)$ the principle reciprocal lattice vectors, and kl are the Miller indices in two dimensions. As shown in Ref. [23] a honeycomb lattice can be described by this amplitude expansion using three terms corresponding to $kl = 10, 01$, and $\bar{1}\bar{1}$ with vectors $\vec{q}_1 = -q_0(\sqrt{3}, 1)/2$ and $\vec{q}_2 = q_0(0, 1)$. The potential of a triangular substrate surface is represented in a similar fashion, i.e., $V = V_0 \sum_{kl} v_{kl} \exp(i\vec{G}_{kl}^s \cdot \vec{r}) + $ c.c., where V_0 is the magnitude of the adhesion strength and $v_{kl} = \exp(i\delta\vec{G}_{kl}^s \cdot \vec{r})$ takes into account the rotation of the substrate with respect to the film. Here $\delta\vec{G}_{kl}^s = \vec{G}_{kl}^{s'} - \vec{G}_{kl}^s$, and $\vec{G}_{kl}^{s'}$ denotes a rotation of the potential through an angle θ, i.e.,

$$\left(\vec{G}_{kl}^{s'}\right)_x = \left(\vec{G}_{kl}^s\right)_x \cos\theta - \left(\vec{G}_{kl}^s\right)_y \sin\theta,$$
$$\left(\vec{G}_{kl}^{s'}\right)_y = \left(\vec{G}_{kl}^s\right)_x \sin\theta + \left(\vec{G}_{kl}^s\right)_y \cos\theta. \quad (1)$$

The APFC free energy functional can then be written as

$$F_\eta = c_A \int d\vec{r} \left[\sum_{kl} \left(B^x |\mathcal{G}_{kl}\eta_{kl}|^2 - \frac{3v}{2}|\eta_{kl}|^4 \right) \right.$$
$$+ \frac{\Delta B}{2} A^2 + \frac{3v}{4} A^4 - 2t \left(\prod_{kl} \eta_{kl} + \text{c.c.} \right)$$
$$\left. + V_0 \left(\sum_{kl} v_{kl}^* \eta_{kl} + \text{c.c.} \right) \right], \quad (2)$$

where $A^2 \equiv 2\sum_{kl}|\eta_{kl}|^2$, $\mathcal{G}_{kl} \equiv \nabla^2 + 2i\alpha\vec{G}_{kl}^f \cdot \vec{\nabla} + 1 - \alpha^2$, and $c_A = 7.95$ eV was chosen to match graphene [31]. The phenomenological parameters $\Delta B, B^x, t$, and v have been discussed in prior publications [30] and take the value $(\Delta B, B^x, t, v) = (0.02, 0.98, -1/2, 1/3)$ in this work. The main parameters of interest here are the misfit strain ε, V_0, and θ which control the elastic energy stored in the film, the film-substrate adhesion energy, and the misorientation, respectively.

In the limit of small displacements this model reduces to a 2D sine-Gordon model that can be solved exactly for the one-dimensional stripe-commensurate transition [23]. In this latter case the free energy can be written as

$$F^{1D} \approx \int d\vec{r} \left[\frac{K}{2} \left(\frac{\partial\Phi}{\partial x} - \varepsilon \right)^2 + W\cos\Phi \right], \quad (3)$$

where x is the coordinate normal to the stripe domain walls, $\Phi = (2k + 1)\pi$ (with k an integer) in the commensurate state and $\Phi = \varepsilon x$ in the incommensurate state, and W and K are the adhesion and elastic energies per unit area. In this limit the system property only depends on the dimensionless ratio W/K, where $W = 4V_0 c_A \phi$ (with $\phi \approx (t - \sqrt{t^2 - 15v\Delta B})/15v)$ and
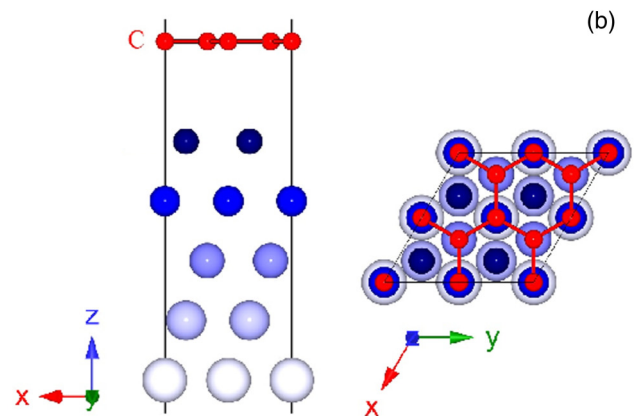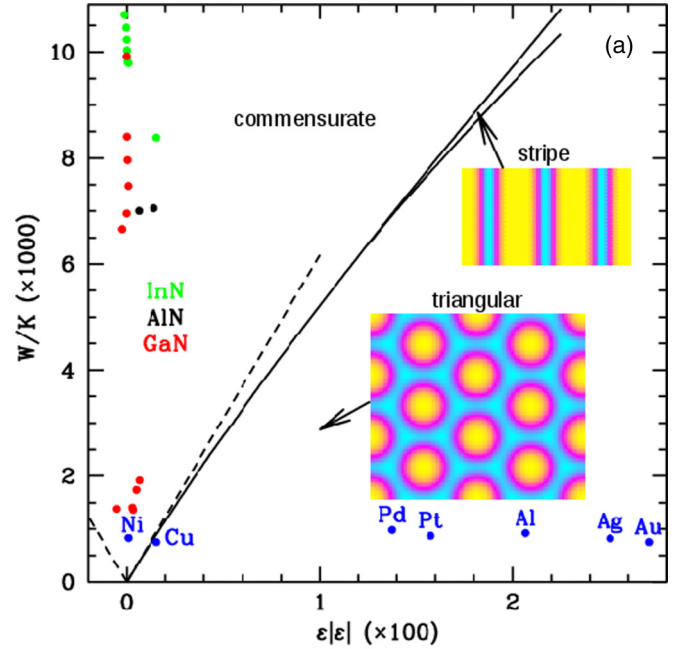

FIG. 1. (a) Phase diagram at zero misorientation, with boundary lines redrawn from APFC calculations in Ref. [23] and blue points determined by the DFT results given in Table I for various graphene/substrate systems. The other points correspond to the DFT data for predictions of 2D III-nitride films on various substrates (given in Appendix A). The color scale in the Moiré patterns is proportional to the local free energy density and the dashed line to $W/K = \pi^2\varepsilon^2/16$. (b) Schematic representation of the slab geometry of graphene adsorbed on the fcc (111) metal substrate, as used in DFT calculations. The red spheres denote carbon atoms, and substrate atom colors and sizes are varied with their distance from the graphene/substrate interface.

$K = (C_{11} + C_{12})^2 / C_{11}$ with C_{ij} the elastic constants. It can be shown that the IC transition from a stripe to commensurate state occurs when $W/K = \pi^2\varepsilon^2/16$ [32].

The full phase diagram of W/K vs misfit strain can be determined from the free energy functional given in Eq. (2). The phase boundaries at zero misorientation have been calculated in Ref. [23] and are redrawn in Fig. 1(a). At small adhesion strengths the lowest energy state corresponds to a 2D Moiré pattern showing as a honeycomb network of domain walls or alternatively a triangular pattern of commensurate

TABLE I. Results of DFT calculations for graphene on various metallic substrates.

substrate (111)	strain (%)	E^c (meV/Å^2)	E^s (meV/Å^2)	W (meV/Å^2)	W/K ($\times 10^{-3}$)
Ni	0.93	−23	1.9	24.9	0.82
Cu	3.92	12	34.4	22.4	0.74
Pd	11.73	222	251.4	29.4	0.97
Pt	12.55	255	281.2	26.2	0.86
Al	14.38	320	347.7	27.7	0.91
Ag	15.83	377	401.6	24.6	0.81
Au	16.45	403	425.4	22.4	0.74

regions if $W/K < \pi^2 \varepsilon^2/16$, and a commensurate state if $W/K > \pi^2 \varepsilon^2/16$. At high ε and W/K there exists a small region between the 2D Moiré pattern and commensurate states in which the stripe phase is the lowest energy state. As discussed before [23] the generic features of the phase diagram (i.e., lack of stripe state at low strains) can be ascribed to the relative energy of domain walls and junctions.

III. DENSITY FUNCTIONAL THEORY CALCULATIONS

In order to match the APFC results with experimental systems of graphene on various fcc (111) substrate surfaces, the ratio W/K was determined via first-principles calculations. The DFT computations were performed with the use of projector-augmented wave method as implemented in the plane-wave code VASP [33–36], employing the vdW-DF-optB88 functional [37–39]. The fcc (111) substrate surfaces were modeled as slabs consisting of five layers, as illustrated in Fig. 1(b). A vacuum of 12 Å is maintained perpendicular to the slab surface to avoid any interaction between the periodic images. The atoms in the bottom three layers were fixed to their bulk positions. An energy cutoff of 650 eV and a k-point mesh of $18 \times 18 \times 1$ result in an accuracy for the total energies within 1 meV/Å^2. The energies per unit area were calculated for (a) a completely commensurate state of graphene on the substrate slab [Fig. 1(b)], E^{tot}, (b) the substrate itself, E^{sub}, (c) a free-standing or completely incommensurate (i.e., $W/K = 0$) graphene layer at the same strain ε, E^{sl}, and (d) a free-standing graphene layer at $\varepsilon = 0$, E^{min}. Defining the graphene strain energy density $E^s = E^{sl} - E^{\text{min}}$ and the commensurate-state energy density $E^c = E^{\text{tot}} - E^{\text{sub}} - E^{\text{min}}$, the adhesion energy per unit area W is then

$$W = E^s - E^c. \qquad (4)$$

The elastic moduli of graphene were also computed by straining the graphene sheet by less than ±0.5% and fitting a polynomial equation of state to the resultant energies. This gives $C_{11} = 352.53$ N/m and $C_{12} = 62.19$ N/m, which are consistent with previous MD [40] and *ab initio* [41] calculations and also experiments [42]. This leads to $K = 30.45$ eV/Å^2. Estimates of W/K are given in Table I for graphene on various metallic substrates.

Using these values of W/K the locations of various graphene/substrate systems in the phase diagram are indicated in Fig. 1(a). With the exception of Ni, all the substrate elements are in the incommensurate 2D triangular region of the phase
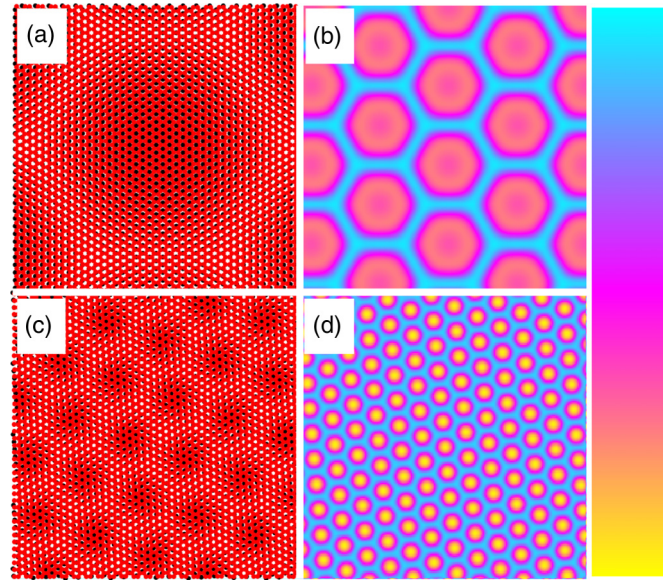

FIG. 2. Sample configurations at $\varepsilon = 3.906\%$ for $\theta = 0°$ and $\theta = 5.36°$ in (a), (b) and (c), (d), respectively. In (a) and (c) the graphene atoms are displayed in red and the surface potential atoms in black, such that commensurate (incommensurate) regions appear red/black (red/white). In (b) and (d) the local free energy density is shown for a 2.71 nm × 2.71 nm portion of the simulation cell. The energy color scale from yellow (low energy) to cyan (high energy) is shown on the right.

diagram, which is consistent with the Moiré patterns that have been observed experimentally. In contrast, for graphene on Ni(111) the value of W/K is in the commensurate region of the phase diagram implying that Moiré patterns should not form, which is also consistent with experiments [43,44]. In addition, these results indicate that the graphene film is only weakly coupled to most metallic substrates other than Cu and Ni, implying that film misorientations are more likely to occur in most systems. The fact that the graphene/Cu system is very close to but below the IC transition line implies a relatively strong coupling strength and a more significant cost for large misorientations of the film Moiré pattern, as verified in the APFC calculations described below (see Figs. 5 and 6).

Figure 1(a) also includes the data points for some single-layer III-nitride materials of 2D honeycomb symmetry on various substrates with triangular-lattice surfaces, based on recent DFT calculations [45,46]. These predictions show that III-V 2D materials would be strongly bound to the substrates, resulting in a commensurate state of the film and the absence of Moiré patterns. The related DFT results are summarized in Appendix A.

IV. ROLE OF FILM/SUBSTRATE MISORIENTATION

The phase diagram shown in Fig. 1(a) was obtained assuming that the film has the same orientation as the substrate surface ($\theta = 0$). To examine the misaligned growth of the film, numerical simulations were conducted to determine the lowest energy states as a function of film-substrate misorientation. Sample portions of configurations are given in Fig. 2 for $\varepsilon = 3.906\%$, and detailed results are presented in
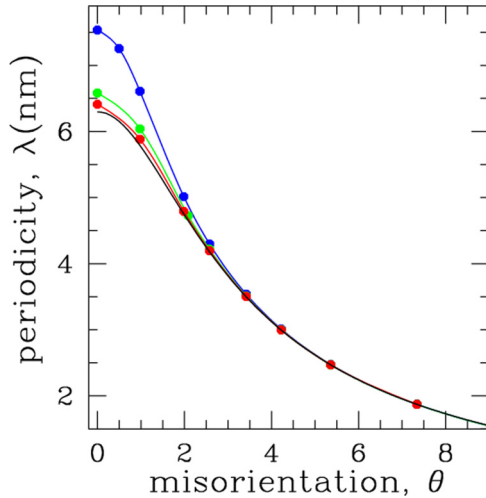
FIG. 3. Periodicity of Moiré patterns as a function of θ for $\varepsilon = 3.906\%$ [as for graphene/Cu(111)], where the blue, green, and red solid points correspond to $W/K = 0.72 \times 10^{-3}$, 0.43×10^{-3}, and 0.29×10^{-3}, respectively. The solid black line corresponds to the $W/K = 0$ limit.

FIG. 4. Periodicity of Moiré patterns as a function of θ for $\varepsilon = 11.19\%$ [as for graphene/Pt(111)], where the magenta, cyan, blue, green, and red solid points correspond to $W/K = 5.75 \times 10^{-3}$, 4.31×10^{-3}, 2.88×10^{-3}, 1.44×10^{-3}, and 0.72×10^{-3}, respectively, and the open circles correspond to the experimental data summarized in Ref. [15]. The solid black line corresponds to the $W/K = 0$ limit.

Figs. 3–6 for two misfit strains of $\varepsilon = 3.906\%$ and 11.19%, corresponding to graphene on Cu(111) and Pt(111) [47], respectively, which represent two distinct limits of relatively strong and weak film-substrate coupling. All the simulations were carried out on a periodic lattice using semispectral methods and depending on θ and ε, contain the equivalence of 3000 to 2.5×10^{10} atomic positions (i.e., 6 nm × 10.4 nm to 19.6 μm × 33.9 μm size systems; see Appendix B). An example of the Moiré patterns simulated is given in Fig. 2, where in (a) and (c) the positions of the film atoms relative to the substrate are illustrated, while in (b) and (d) a comparison of the energy profiles are shown for $\theta = 0°$ and $5.36°$. The pinning is much stronger in the former case as more regions are commensurate with the substrate and the domain walls are much sharper. In the latter case the energy is lower in the commensurate regions (due to lower strain), while the amount of incommensurate regions or domain walls is much greater.

As shown in Figs. 3 and 4, for both misfit strains the periodicity λ of Moiré patterns decreases with increasing misorientation θ and increases with larger W/K. The former dependence can be explained by a simple geometric argument, i.e., at the limit of $W/K = 0$, $\lambda = a_{\text{film}}/\sqrt{\varepsilon^2 + 2(1 - \varepsilon)(1 - \cos\theta)}$ [48], which has been included for comparison. The increase in λ with respect to W/K occurs since a stronger adhesion force leads to larger commensurate regions and a divergence in λ at the IC transition. Also included in Fig. 4 is the experimental data summarized in Merino *et al.* [15] for graphene/Pt(111), consistent with the scenario of a very small adhesion (compared to the IC transition line) predicted in the DFT calculations. The DFT value for Cu(111), 0.74×10^{-3}, is slightly above the largest value (0.72×10^{-3}) examined numerically in Fig. 3, indicating that the periodicity of the corresponding Moiré patterns should be significantly (1–2 nm) larger than that of the zero adhesion limit at small θ. This is consistent with the result of the phase diagram
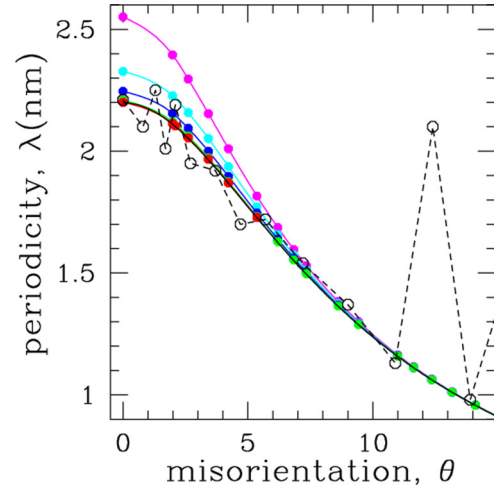
given in Fig. 1(a) which shows that the adhesion strength of graphene/Cu(111) is close to the IC transition.

In Figs. 5 and 6 the free energy difference from the incommensurate state (i.e., $W/K = 0$) per unit area, $\Delta F/A$, is shown for the graphene/Cu(111) and graphene/Pt(111) systems, respectively. The free energy is a smooth function of θ and does not contain special coincident angles for which $\Delta F/A$ dips as suggested by Merino *et al.* [15]. Surprisingly the lowest energy states are at a finite value of θ which corresponds to a smaller periodicity (see Figs. 5 and 6) and correspondingly higher density of domain walls as compared to $\theta = 0$. The misorientation angle for which $\Delta F/A$ is a minimum, θ_{min}, is shown in the insets of Figs. 5 and 6. As

FIG. 5. Free energy density difference for $\varepsilon = 3.906\%$. Color indications are the same as Fig. 3. In the insets θ_{min} is plotted as a function of rescaled adhesion strength. The arrow indicates the value of adhesion strength predicted by DFT.
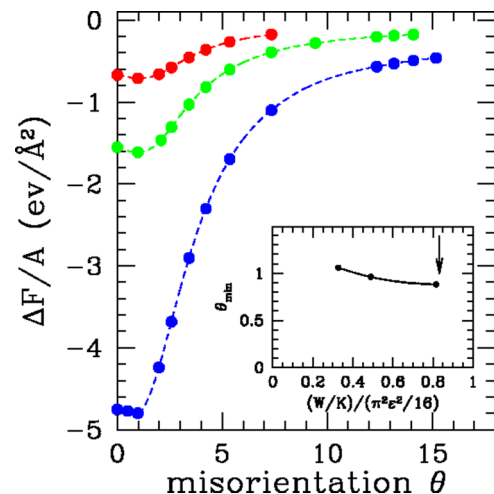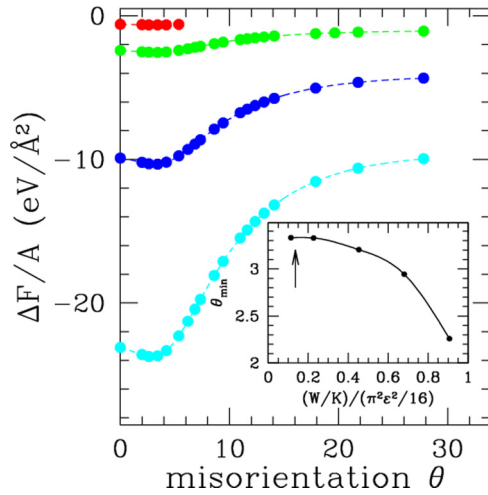
FIG. 6. Free energy density difference for 11.19%. Color indications are the same as Fig. 4. In the insets θ_{min} is plotted as a function of rescaled adhesion strength. The arrow indicates the value of adhesion strength predicted by DFT.

indicated in the figure, given the DFT values of W/K, θ_{min} for the lowest-energy graphene Moiré patterns are approximately $3.22°$ and $0.88°$ for Pt(111) and Cu(111), respectively. This prediction implies a distribution of misorientations with a peak near but not centered at $\theta = 0$ and that the width of the distribution should be broad for graphene/Pt(111) as it is far from the IC transition line, which is consistent with experiments [15]. Since the graphene/Cu(111) system is close to the IC transition, it is likely that the distribution would be

much sharper, as can be deduced from the results of large W/K given in Fig. 5. The related experimental results are mixed, with one group [49] reporting misorientations of only $0°$ and $7°$, others [50,51] reporting only $0°$, and a very recent study obtaining a broader array of misorientations [52], all of which indicate that processing conditions may play an important role. Considering that many substrates (Pd, Al, Ag, Au) are far from the IC line [see Fig. 1(a)], it is expected that they should exhibit properties very similar to that of Pt.

V. SUMMARY

In summary, the competition of film misorientation and substrate adhesion on the ordering of graphene Moiré patterns was examined using an amplitude PFC model and density functional theory. Pattern properties and their variation with film-substrate coupling and mismatch are identified through a classification based on the distance from IC phase transitions. This work shows that the competition leads to an angular dependence of the Moiré pattern periodicity that is consistent with experimental results and also provides predictions for free energy costs of different misorientations. This combination of *ab initio* atomistic calculations with a mesoscopic modeling method provides an efficient and viable route for the quantitative study and predictions of complex growth phenomena on large micron length scales that are typically not accessible using traditional atomistic methods. Given these results it would be worthwhile to extend this combined approach to multicomponent systems for the study of other classes of 2D materials, such as the semiconducting

TABLE II. Calculated quantities for III-V 2D materials from first-principles DFT.

III-V/Substrate	Misfit Strain (%)	E^c (meV/Å^2)	E^s (meV/Å^2)	C_{11} (N/m)	C_{12} (N/m)	W (meV/Å^2)	W/K ($\times 10^{-3}$)
AlN/Zr	3.742	−127.120	13.701	148	69	140.821	7.091
GaN/Zr	−0.264	−137.051	0.277	142	70	137.328	6.952
AlN/Hf	2.522	−133.208	5.789	148	69	138.997	6.999
GaN/Hf	−1.535	−127.585	3.913	142	70	131.498	6.657
InN/Lu	−2.920	−174.124	12.960	98	60	187.084	11.767
InN/Tm	−1.745	−172.010	3.642	98	60	175.652	11.048
InN/Er	−1.087	−168.654	1.539	98	60	170.193	10.704
InN/Ho	−0.555	−165.738	0.502	98	60	166.240	10.456
InN/Dy	−0.122	−162.622	0.099	98	60	162.721	10.234
InN/Tb	0.207	−159.420	0.085	98	60	159.505	10.032
InN/Gd	0.574	−155.768	0.261	98	60	156.029	9.814
InN/Ce	3.923	−122.161	11.169	98	60	133.330	8.386
InN/Y	0.922	−154.781	0.825	98	60	155.606	9.787
GaP/Ce	−3.833	−140.033	6.649	62	21	146.682	21.151
GaN/MoS$_2$	−2.272	−18.588	8.715	142	70	27.303	1.382
GaN/MoSe$_2$	1.686	−25.247	2.534	142	70	27.781	1.406
GaN/NbS$_2$	2.562	−31.206	6.621	142	70	37.827	1.915
GaN/TaS$_2$	2.225	−29.519	4.823	142	70	34.342	1.738
GaN/WSe$_2$	1.786	−24.058	2.889	142	70	26.947	1.364
GaN/ZrB$_2$	−2.544	−231.933	10.253	142	70	242.186	12.260
GaN/HfB$_2$	−3.395	−266.104	17.732	142	70	283.836	14.368
GaN/DyB$_2$	0.883	−147.208	0.443	142	70	147.651	7.474
GaN/ErB$_2$	0.231	−166.040	−0.028	142	70	166.012	8.404
GaN/HoB$_2$	0.580	−157.183	0.054	142	70	157.237	7.959
GaN/TmB$_2$	−0.160	−176.036	0.118	142	70	176.154	8.917

TABLE III. Sample system sizes used in APFC simulations for graphene on a Pt(111) substrate.

Substrate	θ	$L_x \Delta x$	$L_x \Delta x (\mu m)$	$N (\times 10^6)$
Pt(111)	0	2655	0.09	0.5
	1.98458	36287	1.231	100.061
	2.61110	20964	0.711	33.397
	3.42102	12214	0.414	11.336
	4.22104	8024	0.272	4.893
	5.36036	4977	0.169	1.882
	6.19634	3701	0.126	1.041
	7.34100	2655	0.090	0.536
	8.61324	1920	0.065	0.280
	9.43000	1608	0.055	0.196
	11.63506	1063	0.036	0.086
	13.17356	835	0.028	0.053
	14.10536	732	0.025	0.041
	17.89656	439	0.015	0.015
	21.78678	321	0.011	0.008
	27.79578	183	0.006	0.003

TABLE IV. Sample system sizes used in APFC simulations for graphene on a Cu(111) substrate.

Substrate	θ	$L_x \Delta x$	$L_x \Delta x (\mu m)$	$N (\times 10^6)$
Cu(111)	0	2655	0.09	0.5
	0.49744	577528	19.598	25345.894
	0.97770	149501	5.073	1698.438
	1.98458	36287	1.231	100.061
	2.57720	21519	0.730	35.189
	3.42102	12214	0.414	11.336
	4.22104	8024	0.272	4.893
	5.36036	4977	0.169	1.882
	6.19640	3701	0.126	1.041
	7.34100	2655	0.090	0.536
	8.61324	1920	0.065	0.280
	9.42000	1608	0.055	0.196
	11.63506	1063	0.036	0.086
	13.17356	835	0.028	0.053
	14.10536	732	0.025	0.041
	15.17818	624	0.021	0.030

transition metal dichalcogenides, photocatalytic group-IV monochalcogenides, and various III-V monolayers for which their commensurate phase behavior on a variety of substrates has been identified in this work.

APPENDIX A: DFT RESULTS FOR III-V 2D MATERIALS

The quantities needed to calculate the ratio W/K for various physical systems are given in Table II below. These include DFT results for III-V 2D materials on various substrate surfaces that are of triangular symmetry. All the III-V single layers (AlN, GaN, InN, GaP) are of 2D honeycomb structure, while there are three types of triangular substrate surfaces including (i) hcp (0001) for Zr, Hf, Lu, Tm, Er, Ho, Dy, Tb, Gd, Ce, Y, (ii) (0001) surfaces of transition metal dichalcogenides (TMD) MoS_2, $MoSe_2$, NbS_2, TaS_2, WSe_2, and (iii) diboride (0001) with metal cation termination, for ZrB_2, HfB_2, DyB_2, ErB_2, HoB_2, TmB_2. Note that the systems of GaN on TMD substrates (shown as five red points at the bottom-left corner of phase diagram Fig. 1) are metastable as recent DFT calculations show that the adsorption energy is smaller than the energy needed to make single-layer GaN, leading to a large positive formation energy on the substrate, while all other systems can be stabilized as predicted by DFT [45,46].

APPENDIX B: SAMPLE SYSTEM SIZES USED IN APFC CALCULATIONS

In the following Tables III and IV some sample system sizes used in various amplitude PFC simulations for graphene on Pt(111) and Cu(111) substrates are given. In these tables θ is the film-substrate misorientation angle, L_x is the x-direction length of the 2D simulation box (with $L_y = \sqrt{3}L_x$), and N is the corresponding number of atomic positions contained in the box. N is estimated by considering that the area taken up by one graphene atom is $\sqrt{3}a_{\text{graphene}}^2/4$. Larger simulation boxes are needed for smaller θ, as the rotated pattern has to be perfectly periodic within the box due to the periodic boundary condition. Note that $\theta = 0$ can be simulated with smaller system sizes.

[1] E. D. Specht, A. Mak, C. Peters, M. Sutton, R. J. Birgeneua, K. L. D'Amico, D. E. Moncton, S. E. Nagler, and P. M. Horn, Z. Phys. B **69**, 347 (1987).

[2] R. Otero, F. Calleja, V. M. Garcia-Suarez, J. J. Hinarejos, J. de la Figuera, J. Ferrer, A. L. V. de Parga, and R. Miranda, Surf. Sci. **550**, 65 (2004).

[3] K. Pohl, M. C. Bartelt, J. de la Figuera, N. C. Bartelt, J. Hrbek, and R. Q. Hwang, Nature (London) **397**, 238 (1999).

[4] K. Ait-Mansour, A. Buchsbaum, P. Ruffieux, M. Schmid, P. Groning, P. Varga, and R. F. O. Groning, Nano Lett. **8**, 2035 (2008).

[5] K. R. Elder, G. Rossi, P. Kanerva, F. Sanches, S.-C. Ying, E. Granato, C. V. Achim, and T. Ala-Nissila, Phys. Rev. B **88**, 075423 (2013).

[6] K. R. Elder, G. Rossi, P. Kanerva, F. Sanches, S.-C. Ying, E. Granato, C. V. Achim, and T. Ala-Nissila, Phys. Rev. Lett. **108**, 226102 (2012).

[7] C. Gunther, J. Vrijmoeth, R. Q. Hwang, and R. J. Behm, Phys. Rev. Lett. **74**, 754 (1995).

[8] F. E. Gabaly, W. L. W. Ling, K. F. McCarty, and J. de la Figuera, Science **308**, 1303 (2005).

[9] S.-F. Ding, S.-R. Deng, H.-S. Lu, Y.-L. Jiang, G.-P. Ru, D. W. Zhang, and X.-P. Qu, J. Appl. Phys. **107**, 103534 (2010).

[10] A. Wander, C. J. Barnes, L. D. Mapledoram, and D. A. King, Surf. Sci. **281**, 42 (1993).

[11] M. Wasniowska, W. Wulfhekel, M. Przybylski, and J. Kirschner, Phys. Rev. B **78**, 035405 (2008).

[12] J. Jalkanen, G. Rossi, O. Trushin, E. Granato, T. Ala-Nissila, and S.-C. Ying, Phys. Rev. B **81**, 041412 (2010).

[13] A. K. Geim and K. S. Novoselov, Nat. Mater. **6**, 183 (2007).

[14] K. S. Novoselov, V. I. Fal'ko, L. Colombo, P. R. Gellert, M. G. Schwab, and K. Kim, Nature (London) **490**, 192 (2012).

[15] P. Merino, M. Svec, A. L. Pinardi, G. Otero, and J. A. Martin-Gago, ACS Nano **5**, 5627 (2011).

[16] P. Sule, M. Szendro, C. Hwang, and L. Tapaszto, Carbon **77**, 1082 (2014).

[17] P. Sutter, J. T. Sadowski, and E. Sutter, Phys. Rev. B **80**, 245411 (2009).

[18] X. Li, W. Cai, J. An, S. Kim, J. Nah, D. Yang, R. Piner, A. Velamakanni, I. Jung, E. Tutuc, S. K. Banerjee, L. Colombo, and R. S. Ruoff, Science **324**, 1312 (2009).

[19] R. Grantab, V. B. Shenoy, and R. S. Ruoff, Science **330**, 946 (2010).

[20] J. F. Gao, J. Yip, J. J. Zhao, B. I. Yakobson, and F. Ding, J. Am. Chem. Soc. **133**, 5009 (2011).

[21] Z. Sun, S. K. Hamalainen, J. Sainio, J. Lahtinen, D. Vanmaekelbergh, and P. Liljeroth, Phys. Rev. B **83**, 081415(R) (2011).

[22] S. Marchini, S. Günther, and J. Wintterlin, Phys. Rev. B **76**, 075429 (2007).

[23] K. R. Elder, Z. Chen, K. L. M. Elder, P. Hirvonen, S. K. Mkhonta, S.-C. Ying, E. Granato, Z.-F. Huang, and T. Ala-Nissila, J. Chem. Phys. **144**, 174703 (2016).

[24] D. A. C. Brownson and C. E. Banks, *The Handbook of Graphene Electrochemistry* (Springer-Verlag, London, 2014).

[25] Y. Zhu, S. Murali, W. Cai, X. Li, J. W. Suk, J. R. Potts, and R. S. Ruoff, Adv. Mater. **22**, 3906 (2010).

[26] M. J. Allen, V. C. Tung, and R. B. Kaner, Chem. Rev. **110**, 132 (2010).

[27] A. W. Cummings, D. L. Duong, V. L. Nguyen, D. V. Tuan, J. Kotakoski, J. E. B. Vargas, Y. H. Lee, and S. Roche, Adv. Mater. **26**, 5079 (2014).

[28] K. R. Elder, M. Katakowski, M. Haataja, and M. Grant, Phys. Rev. Lett. **88**, 245701 (2002).

[29] K. R. Elder and M. Grant, Phys. Rev. E **70**, 051605 (2004).

[30] K. R. Elder, N. Provatas, J. Berry, P. Stefanovic, and M. Grant, Phys. Rev. B **75**, 064107 (2007).

[31] P. Hirvonen, M. M. Ervasti, Z. Fan, M. Jalalvand, M. Seymour, S. M. Vaez Allaei, N. Provatas, A. Harju, K. R. Elder, and T. Ala-Nissila, Phys. Rev. B **94**, 035414 (2016).

[32] P. M. Chaiken and T. C. Lubensky, *Principles of Condensed Matter Physics* (Cambridge University Press, Cambridge, 1995).

[33] G. Kresse and J. Furthmüller, Phys. Rev. B **54**, 11169 (1996).

[34] G. Kresse and J. Furthmüller, Comput. Mater. Sci. **6**, 15 (1996).

[35] G. Kresse and J. Hafner, Phys. Rev. B **47**, 558 (1993).

[36] G. Kresse and J. Hafner, Phys. Rev. B **49**, 14251 (1994).

[37] J. Klimes, D. R. Bowler, and A. Michaelides, Phys. Rev. B **83**, 195131 (2011).

[38] M. Dion, H. Rydberg, E. Schröder, D. C. Langreth, and B. I. Lundqvist, Phys. Rev. Lett. **92**, 246401 (2004).

[39] G. Román-Pérez and J. M. Soler, Phys. Rev. Lett. **103**, 096102 (2009).

[40] J. Zhou and R. Huang, J. Mech. Phys. Solids **56**, 1609 (2008).

[41] R. Wang, S. Wang, X. Wu, and X. Liang, Physica B **405**, 3501 (2010).

[42] C. Lee, X. Wei, J. W. Kysar, and J. Hone, Science **321**, 385 (2008).

[43] A. Dahal and M. Batzill, Nanoscale **6**, 2548 (2014).

[44] D. Usachov, A. M. Dobrotvorskii, A. Varykhalov, O. Rader, W. Gudat, A. M. Shikin, and V. K. Adamchuk, Phys. Rev. B **78**, 085403 (2008).

[45] A. K. Singh, H. L. Zhuang, and R. G. Hennig, Phys. Rev. B **89**, 245431 (2014).

[46] A. K. Singh and R. G. Hennig, Appl. Phys. Lett. **105**, 051604 (2014).

[47] The lattice constants of Cu and Pt at experimental temperatures are different from that of the zero temperature DFT calculations. Thus the misfit strains used to study the ordering were slightly different than the values summarized in Table I.

[48] S. Tang, H. Wang, Y. Zhang, A. Li, H. Xie, X. Liu, L. Liu, T. Li, F. Huang, X. Xie, and M. Jiang, Sci. Rep. **3**, 2666 (2013).

[49] L. Gao, J. R. Guest, and N. P. Guisinger, Nano Lett. **10**, 3512 (2010).

[50] C. M. Orofeo, H. Hibino, K. Kawahara, Y. Ogawa, M. Tsuji, K.-I. Ikeda, S. Mizuno, and H. Ago, Carbon **50**, 2189 (2012).

[51] L. Zhao, K. T. Rim, H. Zhou, R. He, T. F. Heinz, A. Pinczuk, G. W. Flynn, and A. N. Pasupathy, Solid State Commun. **151**, 509 (2011).

[52] S. Gottardi, K. Muller, L. Bignardi, J. C. Moreno-Lopez, T. A. Pham, O. Ivashenko, M. Yablonskikh, A. Barinov, J. Bjork, P. Rudolf, and M. Stohr, Nano Lett. **15**, 917 (2015).